DISCLAIMER

Isothermal Ice-Crystallization Kinetics in the Gas-Diffusion Layer of a Proton-Exchange-Membrane Fuel Cell

T. J. Dursch,[1,2] M. A. Ciontea,[1] C. J. Radke,[1,2*] A. Z. Weber[2]

[1]Chemical and Biomolecular Engineering Department, University of California, Berkeley, California 94720, United States
[2]Environmental Energy Technology Division, Lawrence Berkeley National Laboratory, Berkeley, California 94720, United States
[3]Earth Sciences Division, Lawrence Berkeley National Laboratory, Berkeley, California 94720, United States

Abstract

Nucleation and growth of ice in the fibrous gas-diffusion layer (GDL) of a proton-exchange membrane fuel cell (PEMFC) are investigated using isothermal differential scanning calorimetry (DSC). Isothermal crystallization rates and pseudo-steady-state nucleation rates are obtained as a function of subcooling from heat-flow and induction-time measurements. Kinetics of ice nucleation and growth are studied at two polytetrafluoroethylene (PTFE) loadings (0 and 10 wt %) in a commercial GDL for temperatures between 240 and 273 K. A nonlinear ice-crystallization rate expression is developed using Johnson-Mehl-Avrami-Kolmogorov (JMAK) theory, in which the heat-transfer-limited growth rate is determined from the moving-boundary Stefan problem. Induction times follow a Poisson distribution and increase upon addition of PTFE, indicating that nucleation occurs more slowly on a hydrophobic fiber than on a hydrophilic fiber. The determined nucleation rates and induction times follow expected trends from classical nucleation theory. A validated rate expression is now available for predicting ice-crystallization kinetics in GDLs.

Key Words: Nucleation, crystallization, kinetics, induction time, differential scanning calorimetry, gas-diffusion layer.

Introduction

Proton-exchange-membrane fuel cells (PEMFCs) show promise in automotive applications because of their high efficiency, high power density, and potentially low emissions. In a PEMFC, reduction of oxygen to water occurs in the cathode. Under subfreezing conditions, water solidifies and hinders access of reactant gases to the catalytic sites in the cathode, thereby severely inhibiting cell performance and possibly causing cell failure.[1] For this reason, understanding the mechanism and kinetics of ice formation is critical to achieving successful cell startup and sustaining high performance at low temperatures.

Because of cell failure under subfreezing conditions, much attention has been given to understanding the fundamentals of cold-start. To date, experimental studies of PEMFC cold-start primarily focus on characterizing overall low-temperature cell performance including: degradation after freeze-thaw cycles[1], effects of cell material properties[2-6], and *in-situ* visualization of ice formation.[7,8] Numerous studies show that the cell electrical potential decays rapidly at low temperatures and/or at high current densities due to ice formation at the reactive area of the cathode.[1-6] Few studies, however, focus on understanding the mechanism of ice crystallization. In two cases, the formation of liquid water and ice within the cathode was visualized using infrared and visible imaging.[7,8] It was shown that water was generated in the subcooled state at −10 °C.[8] Although water did not freeze immediately in the cathode, crystallization kinetics and its dependence on subcooling were not investigated.

Several multiphase, multidimensional cold-start continuum models have been developed.[9,10] These models assume that product water vapor instantaneously solidifies when

the vapor partial pressure exceeds the saturation value. As a result, liquid water within the PEMFC is not accounted for. Recently, cold-start models have been extended to include all phases of water, using the equilibrium Gibbs-Thomson equation to predict freezing-point depressions.[11,12] These models estimate the amount of water and ice in a distribution of pores. However, they invoke instantaneous equilibrium and circumvent the use of a rate equation for ice formation since, at this time, one does not exist for PEMFC media.

Previous work on ice-crystallization kinetics in porous media is also limited in scope with primary applications to frost heave in soils.[13,14] Bronfenbrener and Korin[13,14] experimentally determined kinetic and thermodynamic parameters for ice formation in fine-grained soil. They assumed that the water-crystallization rate is first-order in water content. Other studies of crystallization kinetics in porous media include solidification of water in gel networks and cement pastes, and characterization of polymer-crystallization kinetics in silica gels.[15-18] Because the properties of fuel-cell materials differ considerably from the aforementioned media in wettability, pore size, and microstructure, the proposed crystallization rates are not necessarily applicable.

The goal of the present work is to provide a rate equation for ice formation as a function of ice amount, temperature, and wettability valid within the gas-diffusion layer (GDL) of a PEMFC. Specifically, ice formation is studied within a GDL because this layer retains a significant amount of product water upon cell shutdown.[7, 8] We present a general method for experimentally determining crystallization and nucleation rates using isothermal differential scanning calorimetry (DSC). Further, we develop a nonlinear ice-crystallization rate expression using the Johnson-Mehl-Avrami-Kolmogorov (JMAK) framework that allows extension to the other porous-transport layers within the PEMFC.

Materials and Methods

GDL Characterization. GDLs containing 0 and 10-wt % polytetrafluoroethylene (PTFE) were obtained from Toray (Toray Corp., Tokyo, Japan) and Fuel Cell Earth (FCE, Stoneham, MA), respectively. The FCE GDL is a Toray GDL that contains 10-wt % (PTFE), and GDLs are referred to as GDL(0) and GDL(10), respectively. Relevant material properties are listed in Table 1.

Figure 1 shows scanning-electron-microscopy (SEM) images of a dry GDL(0) (a) and a dry GDL(10) (b). These commercial GDLs are highly porous carbon-fiber papers with porosities ranging from 70 to 90 % and fiber sizes varying between 5 and 10 μm.[19] GDLs are generally treated with nonwetting PTFE to allow for efficient water removal and to prevent flooding. However, addition of PTFE decreases both the medium electrical conductivity and porosity. As a result, there exists a wettability that optimizes overall cell performance.[19]

Sample Preparation. GDL samples were bored into 3.75-mm diameter circles and saturated with Ultrapure Milli-Q® (Millipore, Billerica, MA) distilled/deionized water in a home-built vacuum chamber for 45 min at 4.7 kPa. Excess surface water was blotted with Fisherbrand® (Fisher Scientific, Pittsburg, PA) weighing paper. Water content was determined gravimetrically and measured values were consistent with integrated peak areas generated from DSC. Water loss by evaporation during DSC experiments was determined to be negligible. Additionally, capillary-pressure-saturation measurements show that water does not drain from the GDL interior under atmospheric pressure.[20] Water content was converted to saturation by the expression

$$S = \frac{V_o}{V_p} = \frac{m_l}{m_{dry}} \frac{\rho_{dry}}{\varepsilon \rho_l} \tag{1}$$

where S is liquid-water saturation, V_o is the initial-water volume, V_p is the pore volume, m is mass, ε is porosity, ρ_l is the mass density of water, and ρ_{dry} is the mass density of the dry GDL. Porosities and dry densities were estimated following Lim and Wang.[21] From the material properties in Table 1 and eq 1, GDL water saturations were calculated between 75 and 85%, consistent with the end points of corresponding capillary-pressure-saturation measurements.[20]

Differential Scanning Calorimetry. A PerkinElmer 6000 DSC (PerkinElmer Inc., Waltham, MA) with a liquid-nitrogen chiller measured the heat-flow rate from the sample over time. The DSC was calibrated from the melting points of 99.999% indium (429.78 K) and zinc (692.68 K) (PerkinElmer Inc., Waltham, MA), as well as from dodecane (263.55 K) (Sigma Chemical Co., St. Louis, MO) at lower temperatures. Heat flow to the calorimeter was calibrated using the heat of fusion of indium (28.47 J/g), following Gmelin and Sarge.[22] Nitrogen served as the purge gas at a flow rate of 20 mL/min. Water-saturated GDL samples, weighing between 1 and 5 mg, were placed into 20-μL PerkinElmer hermetically-sealed aluminum pans.

Isothermal crystallization was carried out in the temperature range of 240 to 273 K. Water-saturated GDL samples were placed into the DSC at 300 K and cooled to the desired temperature at 105 K/min. This rapid cooling rate was chosen such that the lowest temperature was reached well before the onset of crystallization. Samples were then held at the subcooled temperature until crystallization was complete. Experiments were performed at two PTFE loadings (0 and 10 wt %) and at various subcoolings, ΔT, defined as the magnitude of the difference in the temperature of freezing and 273 K.

Results

Isothermal Crystallization Kinetics. Figure 2 shows a typical exotherm of heat flow and sample temperature versus time for the GDL(0). Baseline heat flow was adjusted by subtracting the heat measured for the same cycle in an empty furnace. The sample was cooled at 105 K/min to 247 K, where isothermal crystallization commenced (point A in Figure 2). Heat flow due to liberation of the enthalpy of crystallization from point A is evident until a maximum is observed at point B, after which crystallization slows significantly until complete crystallization occurs at point C. To obtain the gas-free volume fraction of ice within the GDL pores, ϕ, as a function of time, crystallization exotherms were integrated from point A to point C according to the expression

$$\phi = \frac{\int_0^t \dot{Q}(t)dt}{\int_0^\infty \dot{Q}(t)dt} \tag{2}$$

where $\dot{Q}(t)$ is the heat-flow rate (mW) from the DSC. Agreement is excellent between total-heat flow for complete crystallization divided by the heat of fusion and the gravimetric water content of the sample. From Figure 2, it is observed that crystallization is preceded by an induction time, τ_i. We define τ_i as the time elapsed between the sample temperature becoming isothermal and the onset of the crystallization peak (point A), about 8 s in Figure 2.

Figures 3 and 4 show the crystallization kinetics, ϕ versus *t*, calculated from eq 2 at three values of ΔT for GDL(0) and GDL(10), respectively. At each subcooling, τ_i was subtracted from the total time so that all curves are compared on a single time scale. Open

symbols represent an average of two exotherms measured for two distinct samples. An integrated exotherm for the GDL(0) at a ΔT of 22 K is included in Figure 4 for ease of comparison (filled triangles). Solid lines in the figures are best least-squares fits to the data as described below. From Figure 4, we observe that at about 20-K subcooling, the time for complete crystallization increases from 9.2 to 14 s for the GDL(0) and GDL(10), respectively. This result suggests that the wettability of the fiber surface plays a role in the crystallization process. More importantly in both figures, the characteristic time for complete crystallization (beyond τ_i) decreases significantly as ΔT increases, indicating that the crystallization rate depends strongly on ΔT.

In many DSC studies, the Avrami relation is adopted to describe crystallization kinetics[23-26]

$$\phi = 1 - \exp\left(-k(T)(t-\tau_i)^n\right) \tag{3}$$

where k is the overall rate constant and n is the Avrami exponent. To obtain k as function of T, eq 3 is fit to the integrated crystallization exotherms in Figures 3 and 4. Based on heat-transfer-limited volume growth, as justified below, we take n = 5/2. Resulting fit values of $k(T)$ from the solid lines in Figures 3 and 4 are listed in Table 2. In agreement with the trends observed in the figures, k increases as ΔT increases and decreases upon addition of PTFE. With n = 5/2, the Avrami equation is in good agreement with integrated exotherms for both GDL(0) and GDL(10).

Induction Time. Repeated crystallization exotherms reveal that τ_i is not constant at a given value of ΔT. To investigate the statistical nature of the crystallization process, τ_i was measured repeatedly (a minimum of 35 measurements) at four values of ΔT. Figure 5 shows 38 induction times measured at subcoolings of (a) 11 K and (b) 22 K, where the dotted line indicates

the number-average induction time, $\bar{\tau}_i$. For both subcoolings, τ_i generally lies below the mean with intermittent excursions to long times. The average induction time decreases significantly from 34.7 s at a subcooling of 11 K to 5.0 s at 22 K. This latter result suggests that similar to the crystallization rate, the induction process also depends strongly on ΔT.

To investigate further the effect of subcooling on τ_i, single induction-time measurements were performed at a number of intermediate values of ΔT. Figure 6 displays τ_i as a function of ΔT for GDL(0). Filled symbols denote a single-τ_i measurement, whereas open symbols represent the number-average induction time, $\bar{\tau}_i$, for at least 35 measurements. Error bars on the open symbols indicate the maximum range of observed τ_i and are included from Figure 5 for reference. The solid line is drawn according to classical nucleation theory (CNT) and is discussed later. As with the data in Figure 5, as ΔT increases, τ_i decreases substantially. Our measured values are qualitatively similar to induction times reported by Heneghan et al.[27] for bulk water and for AgI-seeded water.

To quantify the effect of PTFE on crystallization, similar τ_i measurements were performed on GDL(10). Figure 7 shows a plot of single-τ_i measurements as a function of ΔT for GDL(10) with the results included from Figure 6 for reference. Open symbols reflect GDL(0), whereas closed symbols correspond to GDL(10). The solid, dashed, and dotted lines are from classical nucleation theory (CNT) as discussed below. Addition of PTFE to the carbon-fiber network increases τ_i at nearly all values of ΔT. The GDL(0) curve is identical to the GDL(10) curve, but is shifted to longer ΔT by about 4.5 K. Thus, the formation of ice on hydrophobic fibers commences at a longer induction time for a given subcooling. Similar results have been

reported elsewhere[28,29] showing that the time for complete ice crystallization is longer on a hydrophobic surface than on a hydrophilic surface.

Theory

Parameters k and τ_i in eq 3 are obtained empirically. As shown in Table 2 and in Figures 3 through 7, these parameters are strong functions of both subcooling and wettability. To obtain a predictive rate equation, however, k and τ_i must be specified *a priori*. For this task, we adopt Johnson-Mehl-Avrami-Kolmogorov (JMAK) theory.

Crystallization Kinetics. Within the JMAK framework, crystallization occurs via a continuing two-step process,[23-26] shown schematically in Figure 8. Crystallization begins in Figure 8a with nucleation, during which time a critical nucleus forms at the critical radius, r^*, corresponding to an average nucleation rate, J (nuclei/volume/time), and to a contact angle, θ (measured through the solid phase). Following nucleation, the critical nucleus grows in Figure 8b to a macroscopic size, $r(t)$, during the growth step. This two-step process repeats stochastically until the liquid completely solidifies. At long times, impingement (i.e., size exclusion) of growing nuclei becomes increasingly important. To account for impingement, the so-called Avrami extended or overlapping volume is used, where theoretically overlapping volumes are allowed to grow into remaining free volume. Using this reasoning, JMAK show that in a time, t, the volume fraction of solid transformed, ϕ, is well-described by a convolution integral over nucleation and growth rates[23-26]

$$\phi = 1 - \exp\left(-\frac{4\pi}{3} g(\theta) \int_{\bar{\tau}_i}^{t} J(T(t')) \, r^3(t - t') \, dt' \right) \tag{4}$$

where[30]

$$g(\theta) = \frac{1}{4}(2 + \cos\theta)(1 - \cos\theta)^2, \tag{5}$$

and $J(T)$ is the overall pseudo-steady-state nucleation rate, θ is the contact angle, and $r(t) > r^*$ is the radius of a growing nucleus as a function of time. The explicit time dependence of the nucleation rate is ignored because the time to establish pseudo-steady state nucleation is extremely fast[31]. Eq 5 corresponds to a solid spherical segment growing on a flat surface. A flat surface is a good approximation since the radius of a critical nucleus (nm) is orders of magnitude smaller than the radius of a GDL fiber (μm).

Nuclei described by eq 4 form heterogeneously on GDL fibers at time, t', and grow isotropically in three-dimensions from t' to t. GDLs impregnated with PTFE exhibit hydrophobic patches of coated fibers and hydrophilic regions of uncoated fibers at a geometric scale (μm) much larger than that of the nucleating ice crystals (nm). Therefore, we do not estimate an average contact angle, but rather consider two distinct wetting domains for nucleation. To a first approximation, the overall nucleation rate is a sum of individual nucleation rates on oxidized carbon, J_O, and on PTFE-coated carbon, J_T, weighted by their respective surface-area fractions

$$J = f\, J_T + (1 - f)\, J_O \tag{6}$$

where J is the overall nucleation rate and f is the surface-area fraction of the PTFE coating. Due to the non-uniformity of the PTFE-impregnation process, the surface-area fraction of PTFE is difficult to assess. Consequently, we examine the sensitivity of eq 6 to the choice of f.

Once nuclei form, growth is limited by heat transfer for small Stefan numbers, defined as the ratio of sensible to latent heat[32]

$$Ste = \frac{\hat{C}_{p,l}\Delta T}{\Delta \hat{H}_f} \tag{7}$$

where $\hat{C}_{p,l}$ is the liquid specific heat capacity and $\Delta \hat{H}_f$ is the magnitude of the heat of fusion per mass of solid. For a single heat-transfer-limited growing hemisphere within a subcooled liquid, the so-called Stefan problem[33], the growing solid radius is given by[32]

$$r(t) = 2\eta_o \sqrt{\alpha_l t} \tag{8}$$

where α_l is the liquid thermal diffusivity and η_o is a temperature-dependent growth parameter defined by

$$\eta_o^2 \exp(\eta_o^2)\left[\exp(-\eta_o^2) - \sqrt{\pi}\eta_o \mathrm{erf}(\eta_o)\right] = \frac{1}{2} Ste\,. \tag{9}$$

Eqs 8 and 9 apply strictly at early growth times before single ice crystals impinge and meld with those growing nearby. At later times, precise prediction of the crystal growth rate is not necessary as liquid exhaustion demands a net zero freezing rate.

Substitution of eqs 6 and 8 into eq 4 gives

$$\phi = 1 - \exp\left[-f\, k_T (t - \bar{\tau}_{i,T}^*)^{5/2} - (1-f) k_O (t - \bar{\tau}_{i,O}^*)^{5/2}\right] \tag{10}$$

with

$$k_T(T) = \frac{64\pi}{15} g(\theta_T) J_T \eta_o^3 \alpha_l^{3/2}, \tag{11}$$

and

$$k_O(T) = \frac{64\pi}{15} g(\theta_O) J_O \eta_o^3 \alpha_l^{3/2}, \tag{12}$$

where $\bar{\tau}_i^*$ is a number-average induction time (defined in the subsequent section), with the superscript * representing an induction time in a GDL containing mixed-wetting domains. Subscripts *T* and *O* denote PTFE and oxidized carbon, respectively. To enable a deterministic prediction in eq 10, we replace the single-event induction time appearing in eq 3 by the number-average of the distribution.

Eq 10 does not correspond directly to the Avrami relation in eq 3 used to fit the crystallization kinetics in Figures 3 and 4. However, for GDL(10) and the range of ΔT used in this study, eq 10 simplifies considerably. As shown in detail below, $J_T f << J_O(1-f)$. Hence, the first term in eq 6 and in the exponential argument of eq 10 is negligible. Application of this approximation in eq 10 leads to the Avrami expression in eq 3 with n = 5/2, $k = (1-f)k_O$, and $\tau_i = \bar{\tau}_{i,O}^*$. Therefore, eqs 10 (or 3) and 12 provide the tools to predict the overall crystallization rate once the unknown parameters J_O, θ_O, and $\bar{\tau}_{i,O}^*$ are specified.

Parameter Determination. Eq 12 contains the pseudo-steady-state nucleation rate, J_O. We evaluate J_O from experimental data independent from the measured freezing kinetics in Figures 3 and 4. Jiang and Horst[34] show that the cumulative probability, $P(\tau_{i,O})$, that crystals are detected between time zero and the induction time, $\tau_{i,O}$, is

$$P(\tau_{i,O}) = \frac{M^+(\tau_{i,O})}{M} \tag{13}$$

where M is the total number of experiments and $M^{+}(\tau_{i,O})$ is the number of experiments in which a crystallization peak is detected at an induction time less than or equal to $\tau_{i,O}$. From eq 13, $P(\tau_{i,O})$ is thus available from repeated induction-time measurements. Figure 9 shows the calculated cumulative probability distributions for GDL(0) as open symbols using the data in Figure 5, as well as distributions for two additional values of $\Delta T = 16$ and 30 K.

Jiang and Horst also demonstrate that the cumulative-distribution function is well-described by a Poisson distribution[34]

$$P(\tau_{i,O}) = 1 - \exp\left(-J_O V_o (\tau_{i,O} - \tau_g)\right) \tag{14}$$

where V_o is the initial volume of liquid and τ_g is the time for a critical nucleus to grow to a size detectable by the DSC instrument. Therefore, J_O and τ_g are available by fitting eq 14 to the measured cumulative-probability distributions in Figure 9. Solid lines in this figure correspond to the best least-squares fit of eq 14 and provide values of J_O and τ_g (i.e., the value of P at $\tau_{i,O} = 0$) as functions of ΔT. Obtained values are listed in Table 3, along with the number-average induction time, $\bar{\tau}_{i,O}$. Figure 9 confirms that that the nucleation process in a GDL is well-described by a Poisson distribution.

The dependence of J on ΔT is most often described by classical nucleation theory (CNT)[30,35]

$$J = A \exp\left[-\frac{B}{T(\Delta T)^2} \right] \tag{15}$$

where

$$B = \frac{4\pi\gamma_{sl}^3 T_o^2 \hat{v}_s^2}{3\Delta\hat{H}_f^2 k_b} g(\theta), \tag{16}$$

k_B is the Boltzmann constant, γ_{sl} is the solid/liquid interfacial energy, $\hat{v}_s$ is the specific volume of the solid, T_o is the equilibrium freezing temperature, and $g(\theta)$ is given by eq 5. The pre-exponential factor, A, is assumed to be constant, since its temperature dependence is weak compared to the exponential term.[30,35] The functional dependence of J on ΔT described by eqs 15 and 16 indicates that a plot of $\ln J$ versus $T^{-1}\Delta T^{-2}$ produces a straight line with an intercept $\ln A$ and slope $-B$. The resulting plot is shown in Figure 10 for the J_O values listed in Table 3. The constants, estimated from linear regression, are $A = 7.9\times10^8$ nuclei $\text{m}^{-3}\text{s}^{-1}$ and $B_O = 9.4\times10^4\ \text{K}^3$, which yield an average nucleation rate for GDL(0) of

$$J_O = 7.9\times10^8 \exp\left(\frac{-9.4\times10^4}{T(\Delta T)^2}\right) \text{ nuclei m}^{-3}s^{-1}. \tag{17}$$

Thus, given an estimate of θ_O, $k_O(T)$ is known from eqs 9, 12, and 17. Values for θ are not independently known. We take $\theta_O = 60°$ and $\theta_T = 140°$, as justified below. These contact angles were chosen such that ice preferentially wets oxidized carbon over PTFE; this preference assumes that ice maintains the same relative surface wetting as water against air i.e., the average ice contact angle increases with the addition of PTFE to the GDL.[28,29]

With J_O for GDL(0) now known and the contact angles set, we estimate J_T using eqs 5 and 15-17. From the known value of B_O (eq 17) for GDL(0) with $\theta_O = 60°$, J_T is determined for all ΔT, since A is independent of θ. We find that $B_T = 7.3\times10^5\ \text{K}^3$ for PTFE compared to

$B_O = 9.4\times10^4$ K^3 for oxidized carbon. Accordingly, $J_T / J_O << 1$ and nucleation occurs much more slowly on a hydrophobic surface.

The oxidized-carbon number-average induction time, $\bar{\tau}_{i,O}^*$, appearing in eq 10 remains to be determined. To obtain $\bar{\tau}_i$, the definition suggested by Kaschiev[36] is adopted with slight modification

$$\bar{\tau}_i = \frac{1}{JV_o} + \tau_g . \tag{18}$$

The first term in eq 18 represents the mean time for the formation of a critical nucleus and the second term is included to account for the time elapsed between the formation of a critical nucleus and its growth to a size detectable by the DSC. Values of τ_g lying between those at measured temperatures in Table 3 were obtained by linear interpolation. Let $\bar{\tau}_i^*$ represent the number-average induction time in a GDL containing mixed-wetting regions. Substitution of eq 6 into eq 18 provides the desired expression

$$\bar{\tau}_i^* = \frac{1}{\left(f\,J_T + (1-f)\,J_O\right)V_o} + \tau_g \ . \tag{19}$$

Eq 19 reduces to induction times for nucleation on surfaces of exclusively oxidized carbon, $\bar{\tau}_{i,O}$, and PTFE, $\bar{\tau}_{i,T}$, when $f = 0$ and $f = 1$, respectively. For these cases, the superscript * is omitted because the GDLs each contain a single-wetting domain.

Since $J_T / J_O << 1$, the first bracketed factor in the denominator of eq 19 is negligible provided that $f < 1 - J_T / J_O$. Application of this simplification yields

$$\bar{\tau}_i^* = \bar{\tau}_{i,O}^* \equiv \frac{1}{(1-f)J_O V_o} + \tau_g \qquad \text{for} \quad J_T / J_O << 1 \tag{20}$$

where $\bar{\tau}_{i,O}^*$ denotes the number-average induction time for nucleation only on oxidized carbon in a mixed-wetting GDL. Eq 20 determines $\bar{\tau}_{i,O}^*$ in eq 10. Because nucleation occurs more quickly on oxidized carbon than on PTFE, only $\bar{\tau}_{i,O}^*$ is measured in our work. The solid line in Figure 6 compares $\bar{\tau}_{i,O}^* = \bar{\tau}_{i,O}$ for GDL(0) with theory using eq 20 with $f = 0$. Good agreement is achieved between theory and experiment: the entire temperature dependence is correctly captured through independent assessment of J_O.

Figure 7 shows measured single-induction times for both GDL(0) (open symbols) and GDL (10) (closed symbols). Solid and dash-dotted lines correspond to $\bar{\tau}_{i,O}$ ($f = 0$) and $\bar{\tau}_{i,T}$ ($f = 1$) calculated from eq 19, given the measured value of J_O and the estimated value of J_T. Likewise, dotted and dashed lines are calculations of $\bar{\tau}_{i,O}^*$ from eq 20 with $f = 0.15$ and $f = 0.7$, respectively. Exact positions of the theoretical predictions depend strongly on the choice of J_O for GDL(0). In Figure 7, the average value of J_O is used from Table 3. Since nucleation on the PTFE-coated regions of GDL(10) is negligible in eq 19, the increase in $\bar{\tau}_{i,O}^*$ with f is attributed to the decrease in the available surface-area fraction of oxidized carbon. Dotted $(f = 0.15)$ and dashed lines $(f = 0.7)$ illustrate the sensitivity of $\bar{\tau}_i^*$ to the choice of the surface-area parameter f. Again, the experimental data in Figure 7 are single-τ_i measurements that lie within the Poisson distribution of τ_i. Due to GDL non-uniformity, it is not possible to determine f independently. As a result, it is difficult to assess quantitative agreement between

theory and experiment. Thus in Figure 7, comparison between predicted and measured $\bar{\tau}^*_{i,O}$-values is qualitative. Nevertheless, as f increases, $\bar{\tau}^*_{i,O}$ shifts to longer ΔT, in agreement with measured trends.

Discussion

Comparison to Experiment. With the values of J_O, θ_O, and $\bar{\tau}^*_{i,O}$ now specified, crystallization kinetics, $\phi(t)$, follow from eq 10 for both GDL(0) and GDL(10). In the calculations $k_T = 0$ and k_O obeys eq 12, since $k_O(T) >> k_T(T)$. Additionally, $\bar{\tau}^*_{i,O}$ is given by eq 20 and k_O is calculated using J_O from eq 17 and with $\theta_O = 60°$. Accordingly, eq 10 reduces to the Avrami expression in eq 3.

Figure 11 plots k for GDL(0) (filled circles) and GDL(10) (filled triangles) as a function of ΔT from Table 2. Solid and dashed lines are theoretical predictions of $k = (1-f)k_O$ using eq 12 with $\alpha_l = 1.4\times10^{-7}$ m^2/s, eq 9 for η_o, $f = 0$ for GDL(0), and $f = 0.5$ for GDL(10). Error bars on the theoretical lines represent the range of *k* values calculated using the minimum and maximum nucleation rates as upper and lower bounds. Error increases as ΔT increases because the nucleation rate increases rapidly as ΔT increases. From Figure 11, good agreement is observed between fitted and predicted rate constants, particularly at high values of ΔT (22 and 30 K). Similar to the empirical rate constants in Table 2, *k* increases as ΔT increases. This result is primarily due to the temperature dependence of the nucleation rate. As PTFE is added to the GDL, the decrease in k is quantitatively consistent with experimentally measured values.

Figures 12 and 13 show predicted crystallization kinetics, ϕ versus t, for GDL(0) and GDL(10), respectively. At each subcooling, the single-event induction time was subtracted from the total time so that curves are compared on the same time scale. Open symbols represent an average of two exotherms measured for two distinct samples. Solid lines represent model predictions using calculated k values from Figure 11 in eq 10, with $f = 0$ and $f = 0.5$ for GDL(0) and GDL(10), respectively. Good agreement is seen between theoretical and measured crystallization rates in both Figures 12 and 13. In all cases, the time for complete crystallization is accurately predicted. Crystallization times in Figure 12 range from 5 to 12 s, increasing as subcooling decreases from 30 to 11 K. Dependence of the crystallization time (above induction time) on the amount of subcooling suggests that the controlling resistance for removing heat is at the interface of the growing crystal. Similar to the findings of Feuillebois et al.[37], non-dimensionalizing the ice-crystal/water interface energy balance gives crystallization times in agreement with those found in Figure 12. Thus, the characteristic time for ice crystallization is limited by heat conduction away from the growing ice-crystal front, not by heat conduction out of the sample.

For GDLs of differing water wettability, the time for complete crystallization in Figure 13 increases from 9.2 to 14 s at a ΔT of 20 K for GDL(0) (no PTFE) and GDL(10) (10 wt% PTFE), respectively. Similarly, the predicted time for complete crystallization increases from 9.8 to 14.3 s. Agreement with theory for GDL(10) indicates that, similar to the induction time, the decrease in crystallization rate is a result of the decrease in the available surface-area fraction of oxidized carbon.

Physical Significance. To validate the parameter B, eq 16 was used to estimate the value of the interfacial free energy, γ_{sl}. For $\Delta\hat{H}_f = 335.6\,\text{J/g}$, $\hat{v}_s = 0.916\,\text{g/cm}^3$, $T_o = 273\,\text{K}$, and

$\theta_o = 60°$, γ_{sl} was calculated to be 20 dynes/cm. Although the value for the ice/water interfacial free energy is not directly measureable, commonly cited values[17,27,38] lie between 20 and 45 dynes/cm, indicating reasonable agreement. The determined pre-exponential factor is on the same order of measured nucleation prefactors[27,34,39,40], although it is orders of magnitude smaller than values predicted by CNT (typical CNT prefactors are on the order of 10^{30} nuclei $m^{-3}s^{-1}$)[29]. Experimentally-determined values for A are commonly lower than values predicted by CNT.[27,34,39,40]

To assess the confidence of the reported nucleation rates, a statistical evaluation of the sample size was performed using a power analysis.[41] We estimate that with 90 % confidence and for a sample size of 35, the reported nucleation rate is within 10 % of the actual rate. Because the nucleation rate depends strongly on temperature, temperature fluctuations are expected to be the most prominent source of error. Our DSC provides measurements with a temperature accuracy of ± 0.1 K, which leads to a maximum uncertainty of for example, $2.2 \times 10^7 \pm 1.7 \times 10^6$ nuclei $m^{-3}s^{-1}$ at a ΔT of 10 K.

Relevance to Cold-Start. To illustrate the importance of ice-formation kinetics in automotive cold-start modeling, eqs 10 and 20 were used to estimate the time required for 99% crystallization in GDL(0), $t_{99\%}$, for varying ΔT. A plot of $t_{99\%}$ as a function of ΔT for the GDL(0) is shown in Figure 14. The dotted line estimates the time required for the onset of crystallization (eq 20 with $f = 0$) and the dashed line denotes the time required (from the onset of crystallization) to form 99% of ice (eq 10 with $k_T(T) = 0$ and $k_O(T)$ given by eq 12). The solid line, $t_{99\%}$, is the sum of the dashed and dotted lines. This estimate is drawn using the average value for J_O, neglecting the Poisson distribution of τ_i. $t_{99\%}$ values in Figure 14 are

conservative due to neglect of the thermal mass of the PEMFC, water transport, and the assumption that the temperature instantaneously lowers to the subcooled temperature.

Two limiting regimes for $t_{99\%}$ are shown in Figure 14. At temperatures above 263 K, $t_{99\%}$ is nucleation-rate limited, whereas for temperatures below 263 K $t_{99\%}$ is growth-rate limited. To determine accurately the temperature of transition between the two regimes, however, the entire range of J_O must be included. Nevertheless, because the system is nucleation limited at high temperatures, Figure 14 illustrates that $t_{99\%}$ is on the order of many hours. For example, at 267 K, $t_{99\%}$ is 4.2 hours. This demonstrates that the assumption of instantaneous freezing is not quantitative. As the nucleation rate increases yielding smaller induction times, Figure 14 shows that for 243 K < T < 265 K, $t_{99\%}$ is on the order of a minute. Thus, the commonly-used assumption of equilibrium freezing is more reasonable when the temperature decreases and the system is limited by growth kinetics. Even for $T < 265\,\mathrm{K}$, however, the overall rate constant is far from infinite, suggesting the need to account for crystallization kinetics in understanding cold-start.

Conclusions

We determine pseudo-steady-state nucleation rates and crystallization rates as functions of subcooling in fuel-cell gas-diffusion layers (GDLs) using isothermal differential scanning calorimetry (DSC). Kinetic rates were measured by repeated induction times and heat-flow dynamics for two PTFE loadings (0 and 10 wt%) at temperatures between 240 and 273 K. Induction-time measurements demonstrate that nucleation is well-described by a Poisson distribution and that induction time decreases with increasing subcooling. Experimental

nucleation rates and induction times follow classical nucleation theory. Both induction times and complete crystallization times increase with addition of PTFE to the GDL. Thus, both nucleation and crystal growth occur more slowly on hydrophobic fibers.

Assuming nucleation to a critical radius followed by heat-transfer-limited growth, a nonlinear ice-crystallization rate for GDLs was developed within the JMAK framework. The proposed rate equation is in good agreement with integrated DSC exotherms. Although model crystal growth rates apply specifically to small isolated crystals, the time for complete crystallization is accurately predicted in all cases. The temperature dependence of the crystallization rate is primarily a result of the nucleation rate, consistent with experimental results. As PTFE is impregnated in a GDL, both crystallization rate and induction times decrease because of a reduction in the available surface-area fraction of oxidized carbon. Although the predicted crystallization rate is accurate at subcoolings of 19, 22, and 30K, small deviations are observed at 11 and 13.5 K. These small deviations are thought to be a result of the heterogeneities of the materials and processing, coupled with the stochastic nature of crystallization.

Nomenclature

$\Delta\hat{H}_f$ heat of fusion per mass of solid (kJ/kg)

J pseudo steady-state nucleation rate (nuclei/m^3/s)

k overall rate constant (s$^{-2.5}$)

k_B Boltzmann constant (J/molecule/K)

P cumulative probability

S liquid-water saturation

T Temperature (K)

ΔT subcooling (K)

t time (s)

τ_g time for nuclei grow to an instrument detectable size (s)

$\hat{v}$ specific volume (m^3/kg)

V volume (m^3)

$\dot{Q}$ heat-flow rate (mW)

Greek Letters

α thermal diffusivity (m^2/s)

γ surface tension (dyne/cm)

ε porosity

η_o thermal growth constant

θ contact angle

ρ mass density (kg/m^3)

τ induction time (s)

ϕ volume fraction

Subscripts

o initial

l water

O oxidized carbon

s ice

T PTFE

dry dry gas-diffusion layer

Acknowledgements

This work was funded by the Assistant Secretary for Energy Efficiency and Renewable Energy, Office of Fuel Cell Technologies, of the U. S. Department of Energy under contract number DE-AC02-05CH11231. We thank the Los Alamos National Laboratory for providing the mercury-porosimetry-intrusion data and Haluna Gunterman for providing GDL SEM images.

References

(1) Cho, E.; Ko, J.J.; Ha, H.Y.; Hong, S.A.; Lee, K.Y.; Lim, T.W.; Oh, I.H. *J. Electrochem. Soc.* **2003**, *150*, A1667-A1670.

(2) Oszcipok, M.; Riemann, D.; Kronenwett, U.; Kreideweis, M.; Zedda, M. *J. Power Sources* **2005**, *145*, 407-415.

(3) Tajiri, K.; Tabuchi, Y.; Kagami, F.; Takahashi, S.; Yoshizawa, K.; Wang, CY. *J. Power Sources* **2007**, *165*, 279-286.

(4) Ge, S.; Wang, C.Y. *J. Electrochem. Soc.* **2007**, *154*, B1399-B1406.

(5) Mao, L.; Wang, C.Y. *J. Electrochem. Soc.* **2007**, *154*, B139-B146.

(6) Hishinuma, Y.; Chikahisa, T.; Kagami, F.; Ogawa, T. *Japan Soc. Mech. Eng. Intern.* **2004**, *47*, 235-241.

(7) Ge, S.; Wang, C.Y. *Electrochimica Acta* **2007**, *52*, 4825-4835.

(8) Ishikawa, Y.; Hamada, H.; Uehara, M.; Shiozawa, M. *J. Power Sources* **2008**, *179*, 547-552.

(9) Mao, L.; Wang, C.Y.; Tabuchi, Y. *J. Electrochem. Soc.* **2007**, *154*, B341-B351.

(10) Meng, H. *J. Power Sources* **2008**, *178*, 141-150.

(11) Jiao, K.; Li, X. *Electrochimica Acta* **2009**, *54*, 6876-6891.

(12) Balliet, R.; Newman, J. *J. Electrochem. Soc.* **2011**, *158*, B927-B938.

(13) Bronfenbrener, L.; Korin, E. *Intern. J. Mass Transfer* **1997**,*40*, 1053-1059.

(14) Bronfenbrener, L.; Korin, E. *Chem. Eng. and Processing* **2002**, *41*, 357-363.

(15) Zhang, H.; Banfield, J. *Chemistry of Materials* **2002**, *14*, 4145-4154.

(16) Kim, S.H.; Ahn, S.H., Hirai, T. *Polymer* **2003**, *44*, 5625-5634.

(17) Scherer, G.W. *J. Non-Crystalline Solids* **1993**, *155*, 1-25.

(18) Fen-Chong, T.; Fabbri, A. *C. R. Mecanique* **2005**, *333*, 425-430.

(19) Luo, G.; Ji, Y.; Wang, C.Y.; Sinha, P.K. *Electrochimica Acta* **2010**, *55*, 5332-5341.

(20) Gostick, J. T.; Fowler, M. W.; Ioannidis, M. A.; Pritzker, M. D.; Volfkovich, Y. M.; Sakars, A. *J. Power Sources* **2006**, *156*, 375-387.

(21) Lim, C.; Wang, C.Y. *Electrochimica Acta* **2004**, *49*, 4149-4156.

(22) Gmelin, E.; Sarge, St. M. *Pure and Appl. Chem.* **1995**, *67*, 1789-1800.

(23) Avrami, M. *J. Chem. Phys.* **1939**, *7*, 1103-1112.

(24) Avrami, M. *J. Chem.Phys.* **1940**, *8*, 212-224.

(25) Johnson, W.A.; Mehl, R.F. *Trans. AIME **1939**,* 135*, 416.*

(26) Kolmogorov, A.N. *Ser. Math.* **1937**, *3*, 335.

(27) Heneghan, A. F.; Wilson, P. W.; Haymet, A. D. J. *PNAS* **2002**, *99*, 9631-9634.

(28) Suzuki, S.; Najajima, A.; Yoshia, N.; Okada, K. et al. *Chem. Phys. Lett.* **2007**, *445*, 37-41.

(29) Vollhardt, D.; Ziller, M.; Retter, U. *Langmuir* **1993**, *9*, 3208-3211.

(30) Uhlman, U.D.; Chalmers, B. *Nucleation Symposium* **1965**, *57*, 19-31.

(31) Kashchiev, D. *Nucleation: Basic Theory with Applications*, 1st ed.; Butterworth-Heinemann: Oxford, 2000; Chapter 15.

(32) Carslaw, H.S.; Jaeger, J.C. *Conduction of Heat in Solids*, 2nd ed.; Oxford University Press: Oxford, 1959; Chapter 11.

(33) Rubinstein, L. I. *The Stefan Problem*; AMS, Providence, Rhode Island , 1971; Chapter 1.

(34) Jiang, S.; Horst, J. H. *Crystal Growth and Design* **2011**, *11*, 256-261.

(35) Turnbull, D.; Fisher, J.C. *J. Chem. Phys.* **1949**, *17*, 71-73.

(36) Kashchiev, D. *J. Crystal Growth* **1991**, *110*, 373-380.

(37) Feuillebois, F.; Lasek, A.; Creismeas, P.; Pigeonneau, F.; Szaniawski, A. *J. Colloid and Interface Science* **1995**, *169*, 90-102.

(38) Hardy, S. C. *Philosophical Magazine* **1977**, *35*, 471-484.

(39) Laval, P.; Crombez, A.; Salmon, J.B. *Langmuir* **2009**, *25*, 1836-1841.

(40) Paul, B. K.; Joshi, M. S. *J. Phys. D: Appl. Phys.* **1976**, *9*, 1253-1256.

(41) Lachin, J. M. *Controlled Clinical Trials* **1981**, *2*, 93-113.

Table 1.

GDL Properties

GDL	Thickness (μm)	PTFE (wt %)	Porosity, ε	Water Saturation, S
GDL(0)	190	0	[a]80.0 %	[b]84±3 %
GDL(10)	190	10	[a]72.8 %	[b]78±2 %

[a] Mercury-intrusion-porosimetry data provided by Los Alamos National Laboratory.
[b] From eq 1

Table 2.

Crystallization Rate Constant, *k*, for GDL(0) and GDL(10)

GDL(0), k ($s^{-2.5}$)	**GDL(10), k ($s^{-2.5}$)**	**Subcooling, ΔT (K)**
0.009	-	11
-	0.008	13.5
-	0.017	19
0.023		20
0.029	-	22
0.053	-	30

Table 3.

Nucleation Rates, Average Induction Times, and Growth Times for GDL(0)

Subcooling, ΔT (K)	**Nucleation Rate, J_O ($\times 10^{-7}$ nuclei $m^{-3}s^{-1}$)**	**Induction Time, $\bar{\tau}_{i,O}$ (s)**	**Growth Time, τ_g (s)**
11	3.3	34.7	7.5
16	12.0	14.3	4.2
22	40.0	5.0	0.7
30	63.0	2.7	0.6

Figure Captions

Figure 1. SEM images of the GDL(0) (a) and the GDL(10) (b). Both are Toray carbon papers that have either 0 or 10-wt % PTFE, respectively.

Figure 2. Typical isothermal DSC cooling exotherm of GDL(0) at 247 K. The solid line corresponds to the sample temperature, whereas the dotted line represents heat flow. The symbol τ_i labels the induction time. A-C label the onset, extremum, and completion of water freezing, respectively.

Figure 3. Isothermal freezing kinetics for GDL(0), containing 0-wt % PTFE, at three subcoolings. Solid lines represent best least-squares fits of eq 3 to the experimental data.

Figure 4. Isothermal freezing kinetics for GDL(10) containing 10-wt% PTFE at two subcoolings (open symbols). Closed symbols represent GDL(0), containing 0-wt % PTFE for comparison. Solid lines represent best least-squares fits of eq 3 to the experimental data.

Figure 5. 38 induction-time measurements at a subcooling of (a) 11 K and (b) 22 K for GDL(0). A dotted line indicates the number-average induction time.

Figure 6. Induction times as a function of subcooling for GDL(0). Filled symbols are single induction-time measurements $\left(\tau_{i,O}\right)$, whereas open symbols represent the number-average induction times over a minimum of 35 measurements $\left(\bar{\tau}_{i,O}\right)$. Error bars indicate the maximum range of observed induction times. The solid line is a prediction for $\bar{\tau}_{i,O}$ from classical nucleation theory (CNT).

Figure 7. Induction times as a function of subcooling for GDL(0) (open symbols) and GDL(10) (closed symbols). Solid, dotted, and dashed lines are predictions for $\bar{\tau}_i^*$ from CNT (eq 20) for nucleation on oxidized carbon fibers at varying f, where f is the surface-area fraction of PTFE in the GDL. The dash-dotted line is a prediction for $\bar{\tau}_i^*$ from CNT (eq 19) for nucleation on completely PTFE-coated fibers.

Figure 8. Schematic of the continuous two-step crystallization process occurring within a subcooled liquid: (a) nucleation and (b) growth with continuing nucleation. r^* is the critical nucleation radius, and θ is the contact angle of the ice/water/substrate triple line measured through solid ice.

Figure 9. Cumulative probability distributions for the induction times shown in Figure 5 for GDL(0) along with two additional subcoolings at $\Delta T = 16$ and 30 K. Sold lines are a fit to the probability distribution in eq 14.

Figure 10. Logarithm of the nucleation rate in GDL(0) as a function of $T^{-1}\Delta T^{-2}$ for the values given in Table 3. The intercept of the straight line gives ln$A$ and the slope gives $-B_O$, following eqs 15 and 16.

Figure 11. Overall rate constant, k, for GDL (0) (filled circles) and GDL(10) (filled triangles) as a function of subcooling. Filled symbols correspond to fitted values from eq 3. Solid and dashed lines are theoretical predictions of $k=(1-f)k_O$ with $\alpha_l = 1.4\times10^{-7}\,\mathrm{m^2/s}$, $\theta_O = 60°$, an average value for J_O, and $f=0$ and $f=0.5$ for GDL(0) and GDL(10), respectively. Error bars on lines indicate the range of calculated k using the minimum and maximum J_O obtained from Figure 6.

Figure 12. Isothermal freezing kinetics for the GDL(0) at three subcoolings. Solid lines represent theoretical predictions of ϕ using eq 10 and eq 12 for $k_O(T)$ with $\alpha_l = 1.4\times10^{-7}\,\mathrm{m^2/s}$, $\theta_o = 60°$, J_O from eq 17, η_o from eq 9, and $f=0$.

Figure 13. Isothermal freezing kinetics for the GDL(10) at two subcoolings. Solid lines represent theoretical predictions of ϕ using eq 10 and eq 12 for $k_O(T)$ with $\alpha_l = 1.4\times10^{-7}\,\mathrm{m^2/s}$, $\theta_o = 60°$, J_O from eq 17, and η_o from eq 9, and $f=0.5$.

Figure 14. Time required for 99% crystallization as a function of temperature for the GDL(0). The dotted line estimates time required for the onset of crystallization, given by eq 19 with $f=0$. The dashed line represents the time required (from the onset of crystallization) to form 99% of ice using eq 10 with $k_T(T)=0$ and $k_o(T)$ given by eq 12. The solid line is the sum of the two dotted lines.

a)

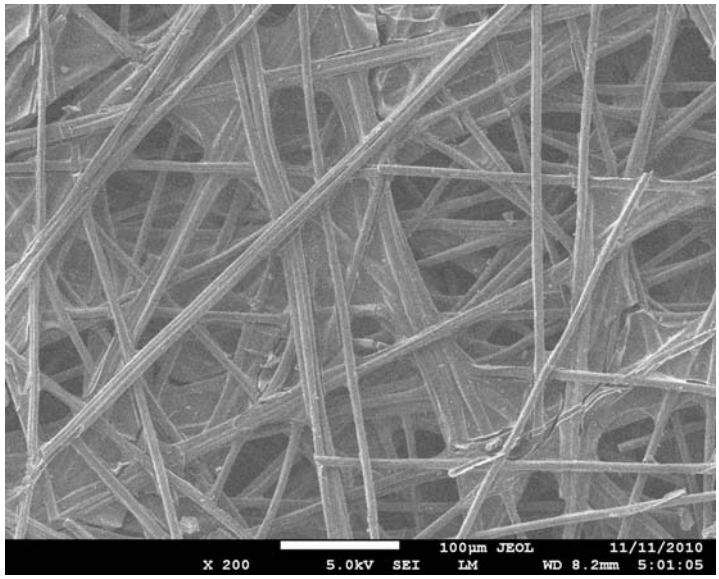

b)

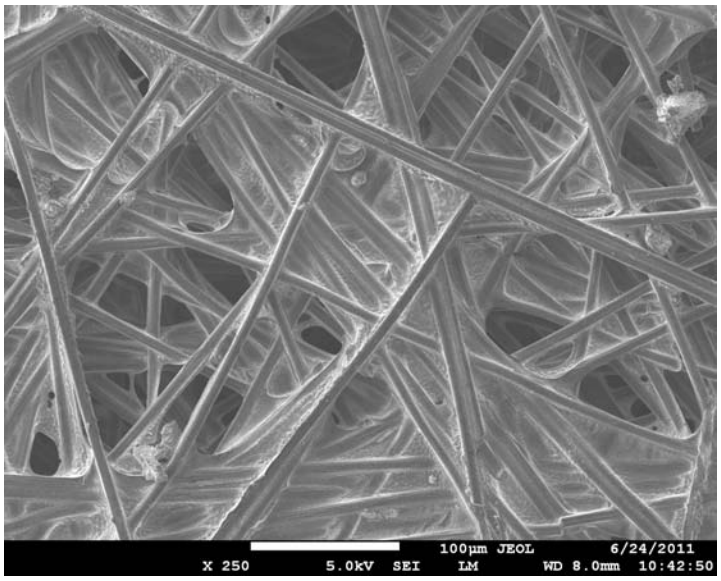

Figure 1. SEM images of the GDL(0) (a) and the GDL(10) (b). Both are Toray carbon papers that have either 0 or 10-wt % PTFE, respectively.

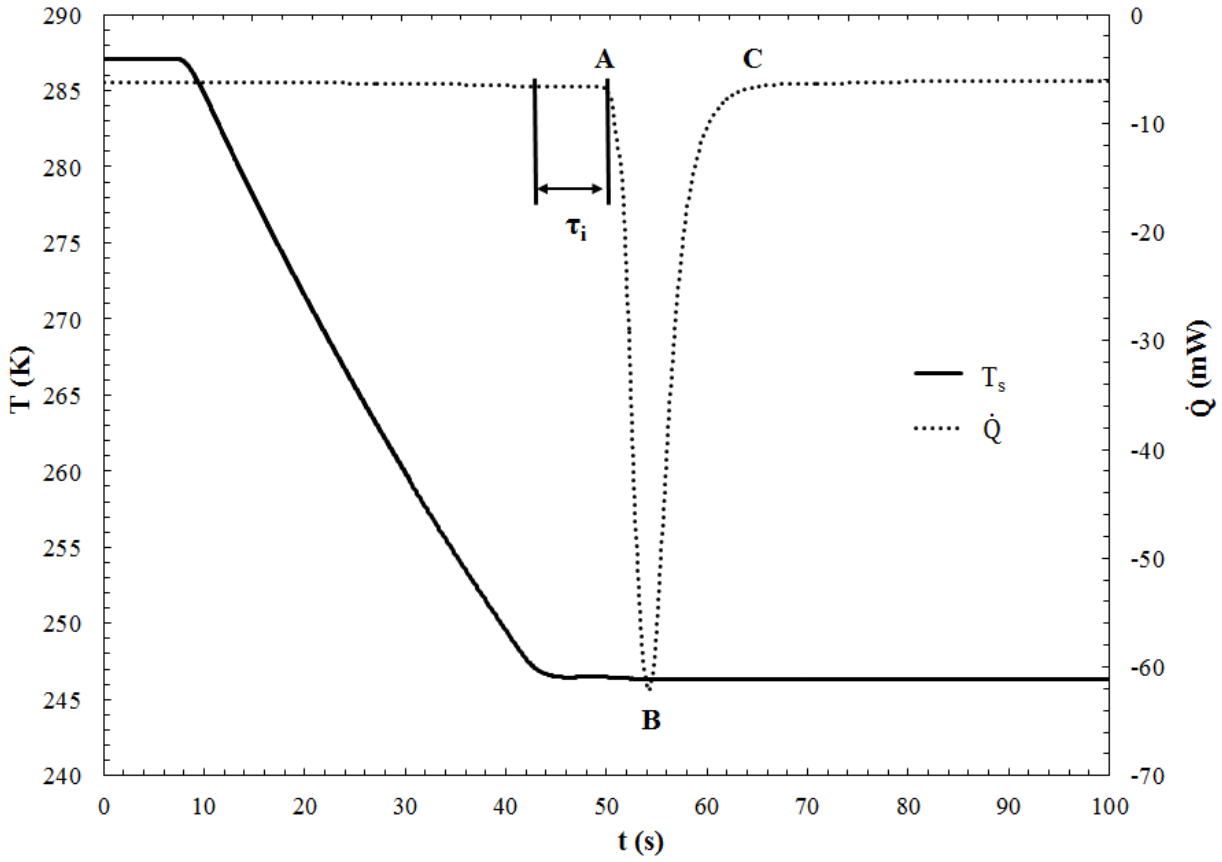

Figure 2. Typical isothermal DSC cooling exotherm of GDL(0) at 247 K. The solid line corresponds to the sample temperature, whereas the dotted line represents heat flow. The symbol τ_i labels the induction time. A-C label the onset, extremum, and completion of water freezing, respectively.

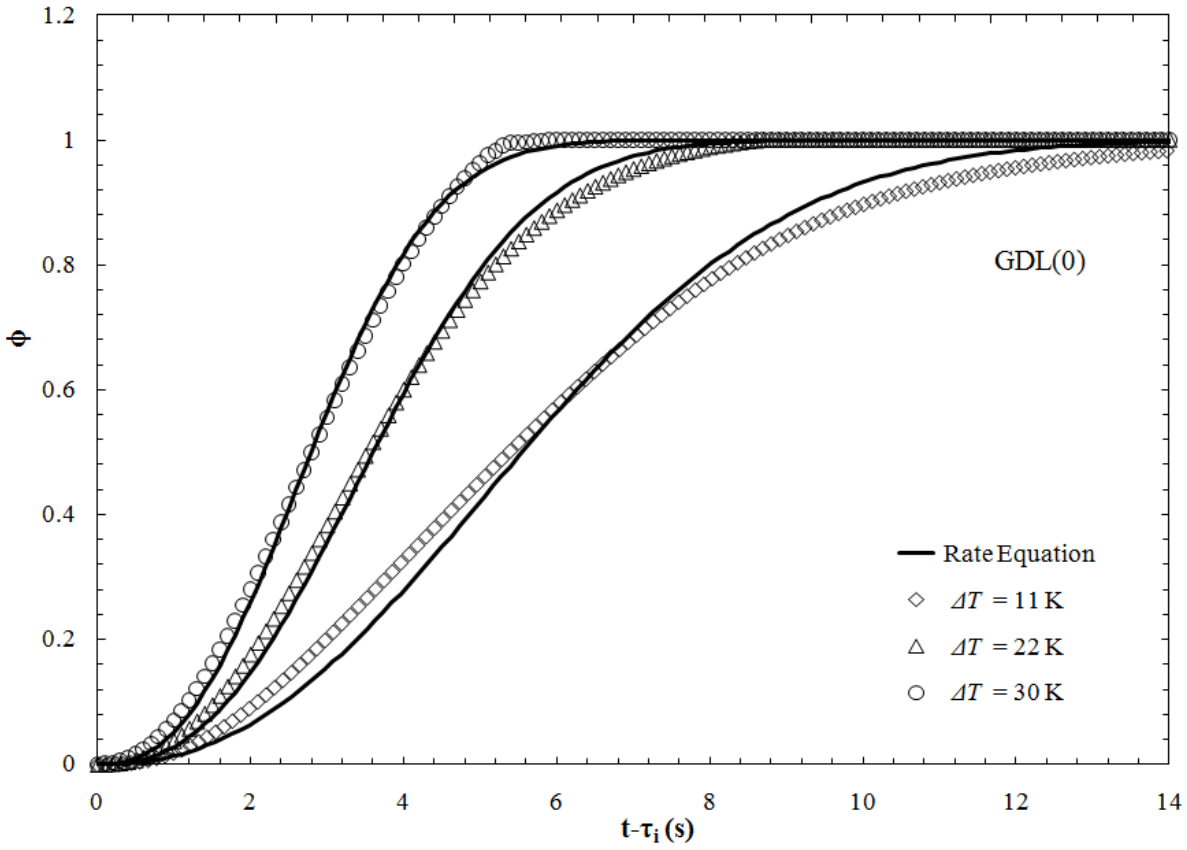

Figure 3. Isothermal freezing kinetics for GDL(0), containing 0-wt % PTFE, at three subcoolings. Solid lines represent best least-squares fits of eq 3 to the experimental data.

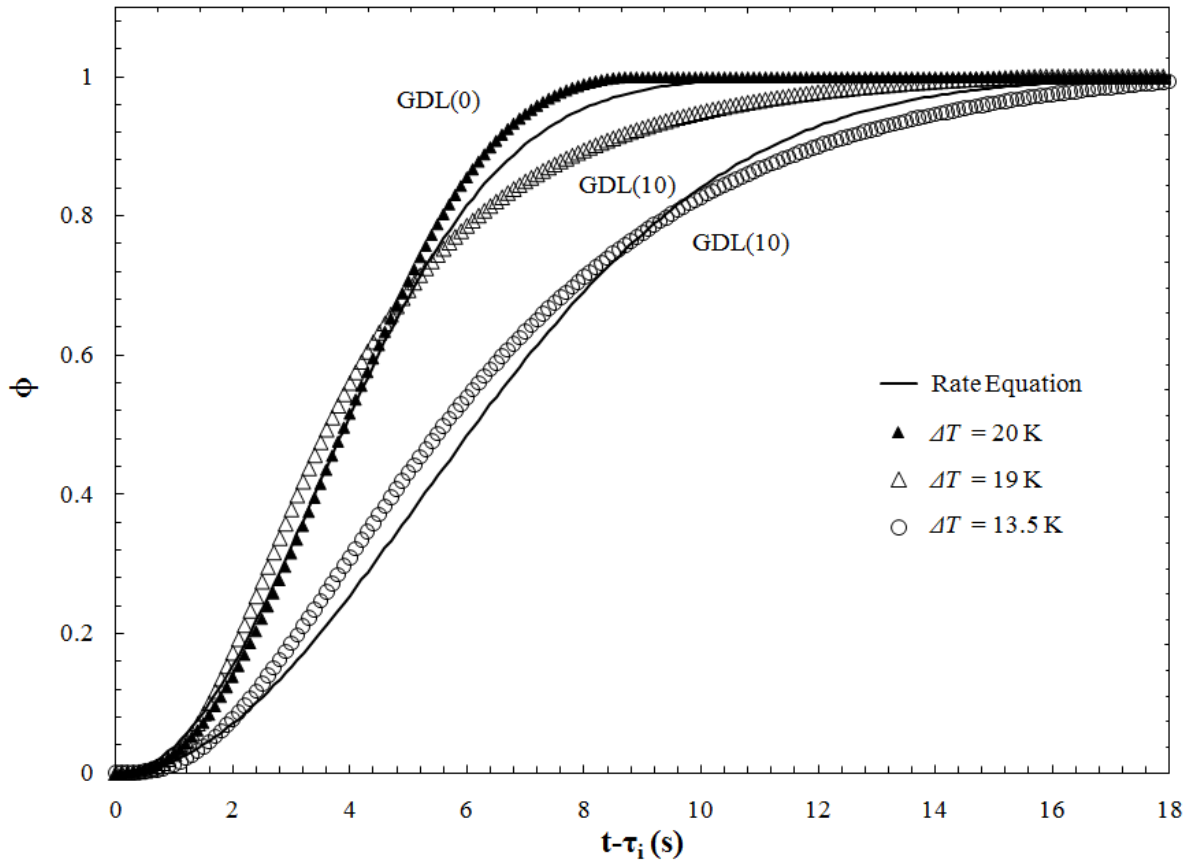

Figure 4. Isothermal freezing kinetics for GDL(10) containing 10-wt% PTFE at two subcoolings (open symbols). Closed symbols represent GDL(0), containing 0-wt % PTFE for comparison. Solid lines represent best least-squares fits of eq 3 to the experimental data.

a)

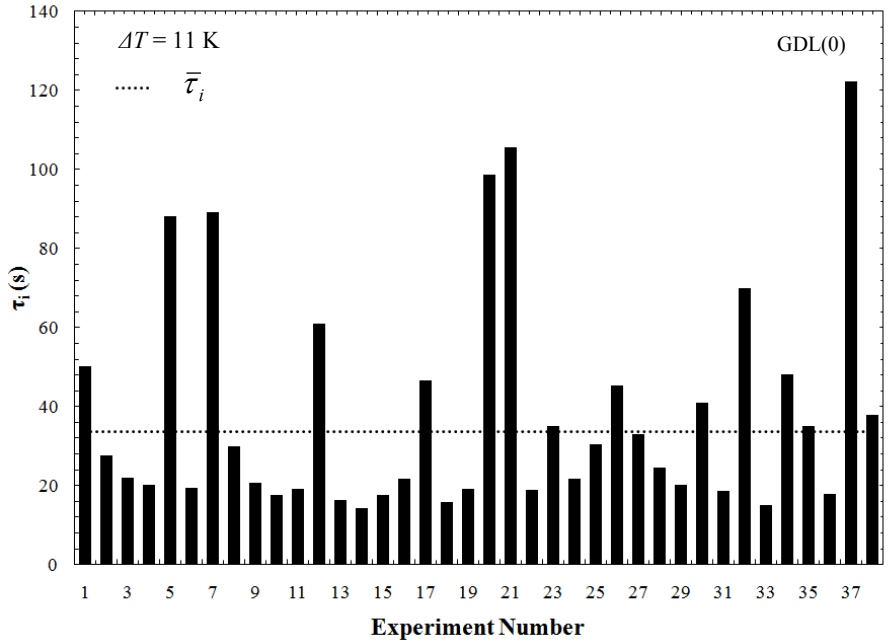

b)

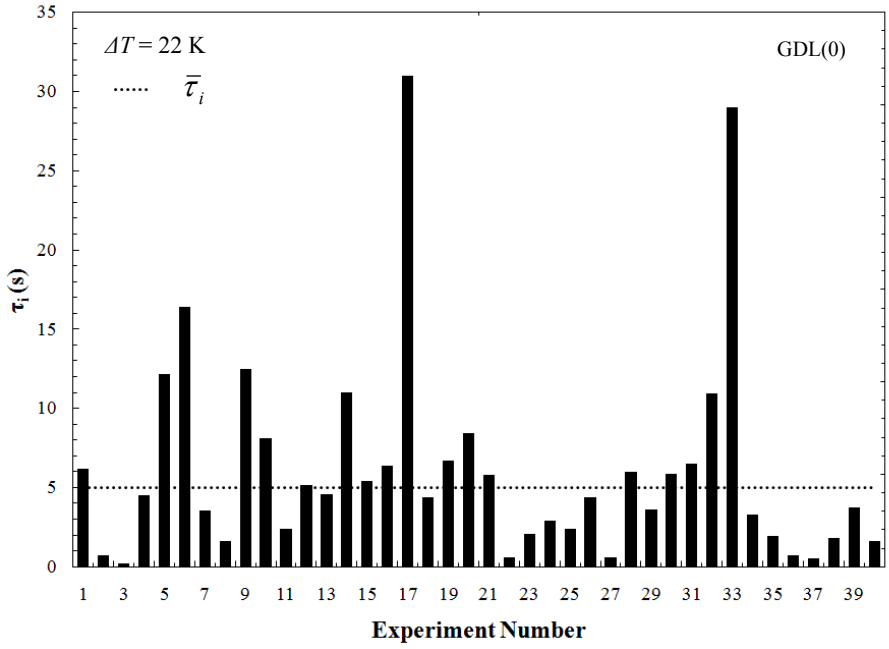

Figure 5. 38 induction-time measurements at a subcooling of (a) 11 K and (b) 22 K for GDL(0). A dotted line indicates the number-average induction time.

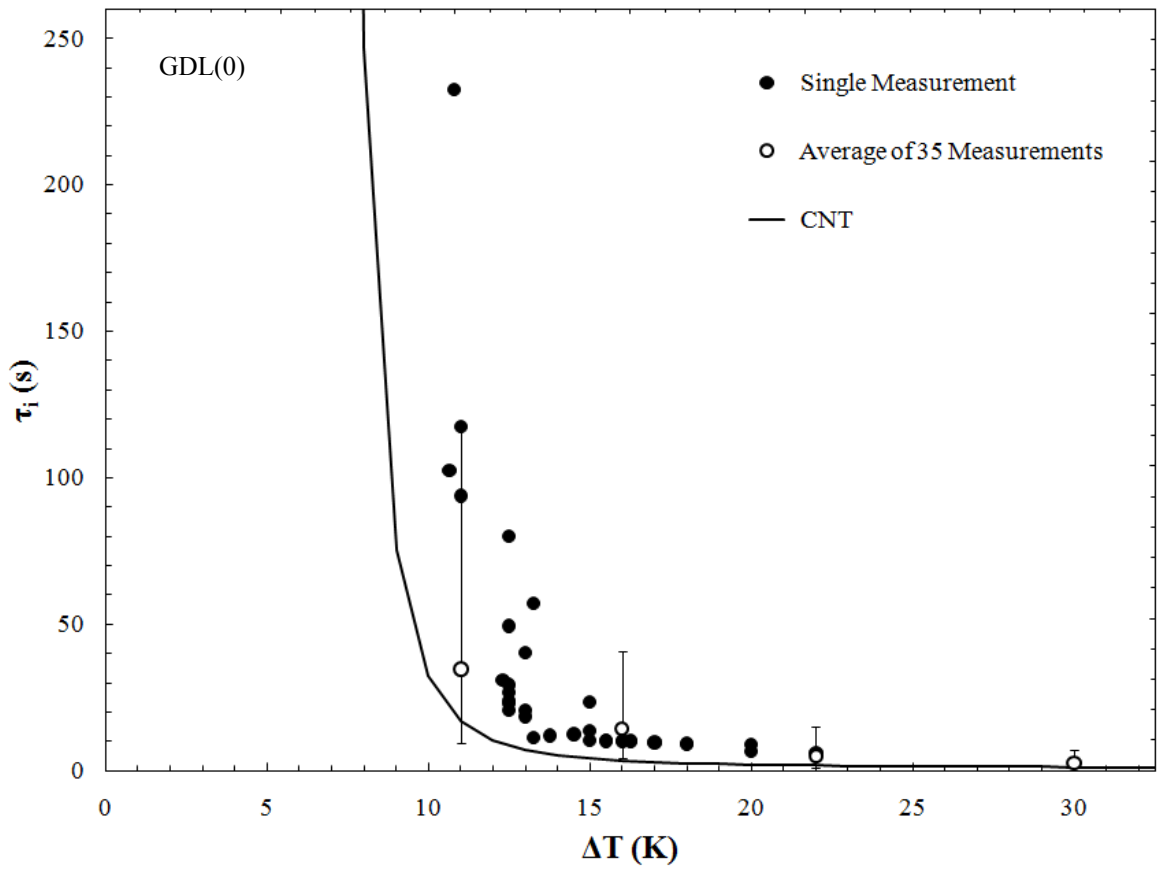

Figure 6. Induction times as a function of subcooling for GDL(0). Filled symbols are single induction-time measurements $(\tau_{i,O})$, whereas open symbols represent the number-average induction times over a minimum of 35 measurements $(\bar{\tau}_{i,O})$. Error bars indicate the maximum range of observed induction times. The solid line is a prediction for $\bar{\tau}_{i,O}$ from classical nucleation theory (CNT).

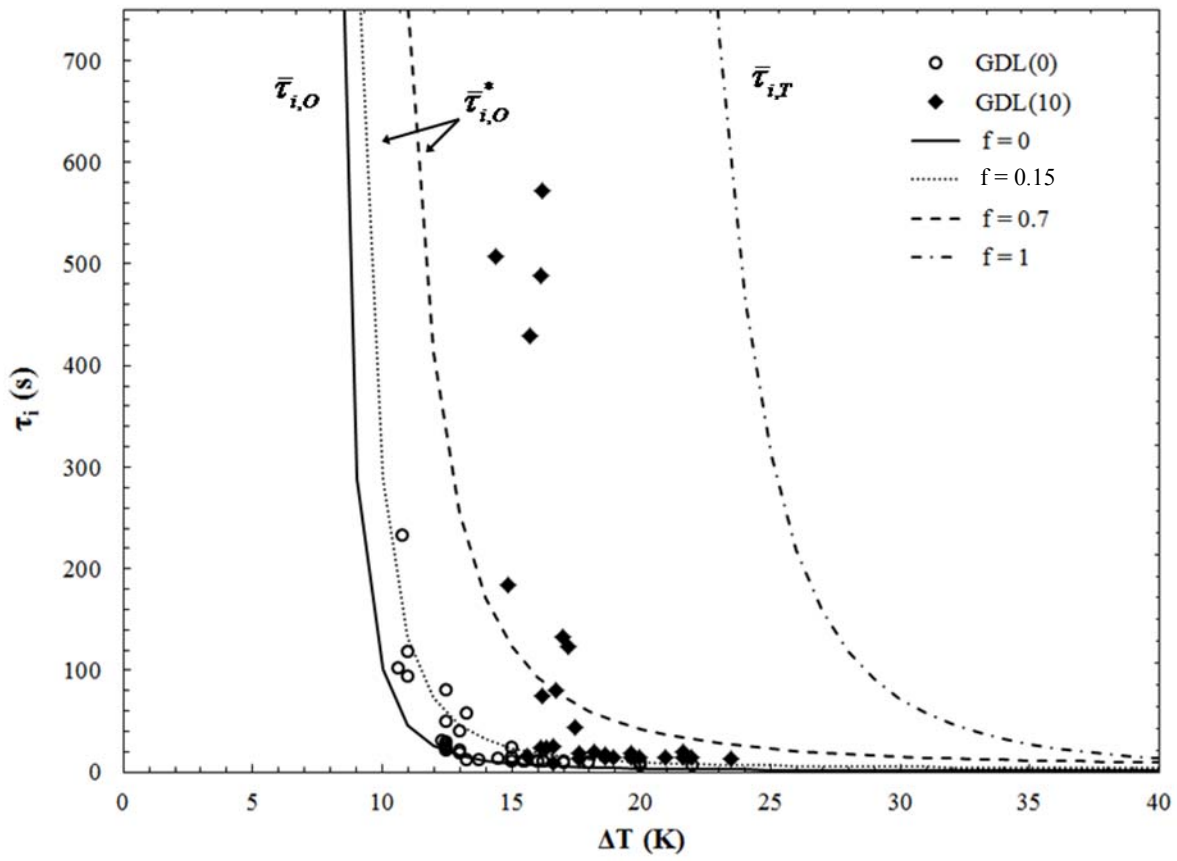

Figure 7. Induction times as a function of subcooling for GDL(0) (open symbols) and GDL(10) (closed symbols). Solid, dotted, and dashed lines are predictions for $\bar{\tau}_i^*$ from CNT (eq 20) for nucleation on oxidized carbon fibers at varying f, where f is the surface-area fraction of PTFE in the GDL. The dash-dotted line is a prediction for $\bar{\tau}_i^*$ from CNT (eq 19) for nucleation on completely PTFE-coated fibers.

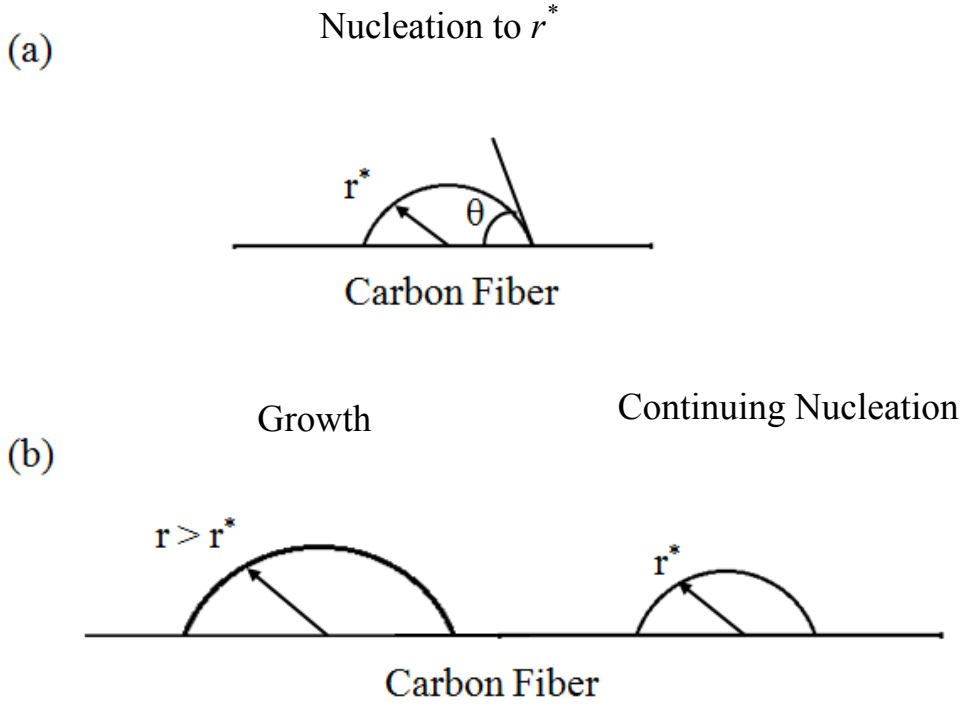

Figure 8. Schematic of the continuous two-step crystallization process occurring within a subcooled liquid: (a) nucleation and (b) growth with continuing nucleation. r^* is the critical nucleation radius, and θ is the contact angle of the ice/water/substrate triple line measured through solid ice.

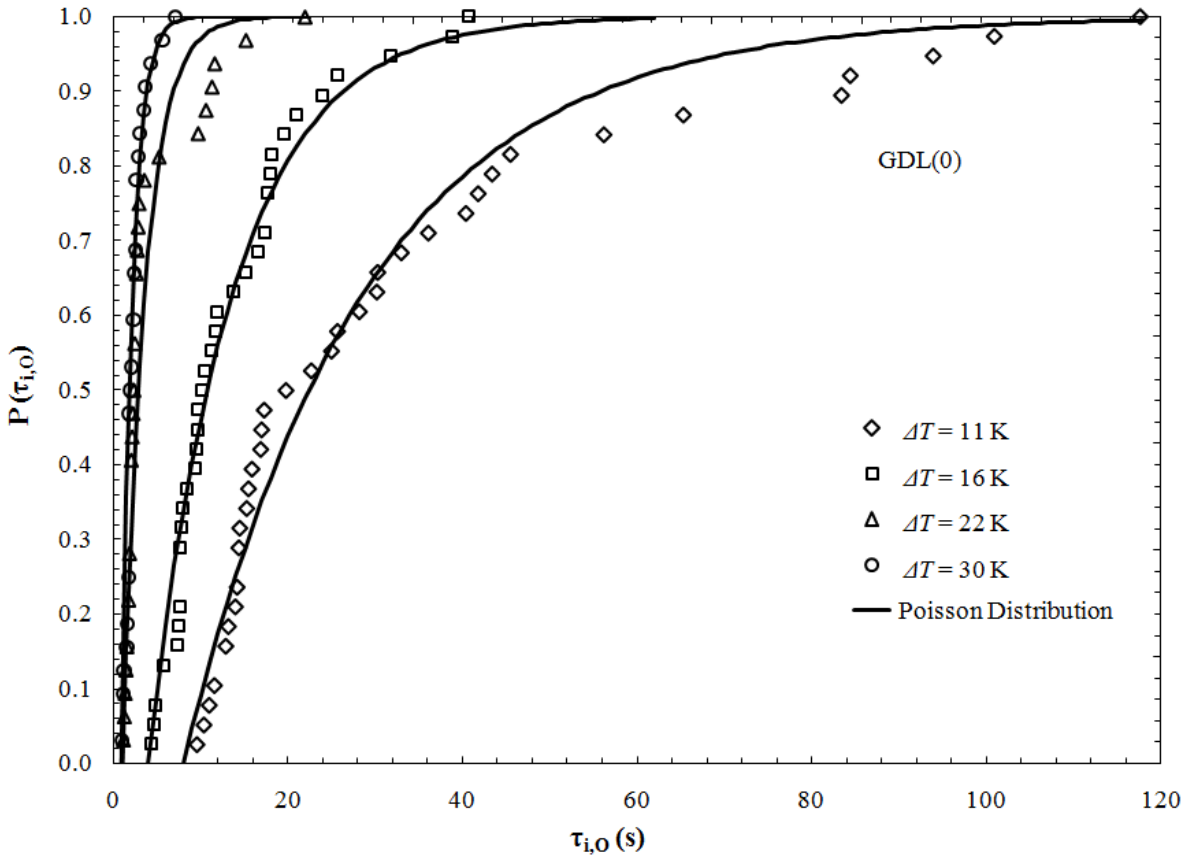

Figure 9. Cumulative probability distributions for the induction times shown in Figure 5 for GDL(0) along with two additional subcoolings at $\Delta T = 16$ and 30 K. Sold lines are a fit to the probability distribution in eq 14.

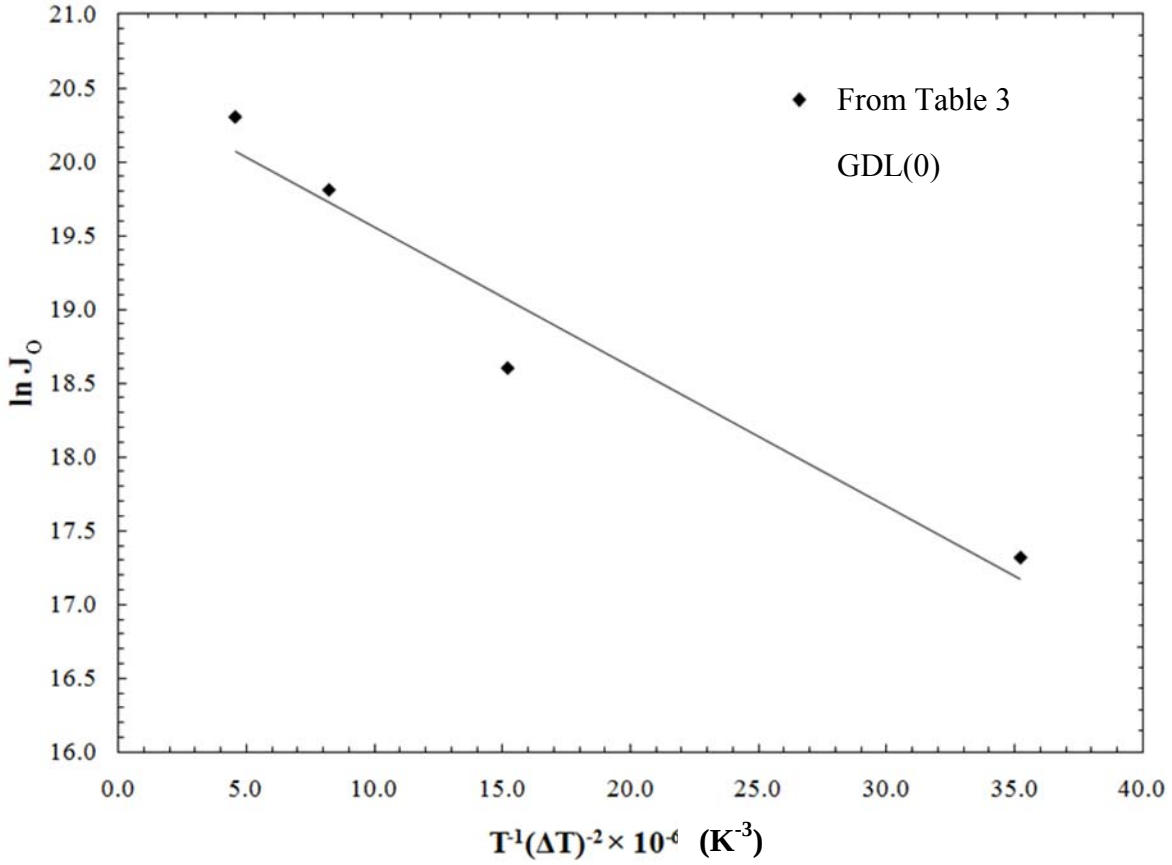

Figure 10. Logarithm of the nucleation rate in GDL(0) as a function of $T^{-1}\Delta T^{-2}$ for the values given in Table 3. The intercept of the straight line gives ln$A$ and the slope gives $-B_O$, following eq 15 and 16.

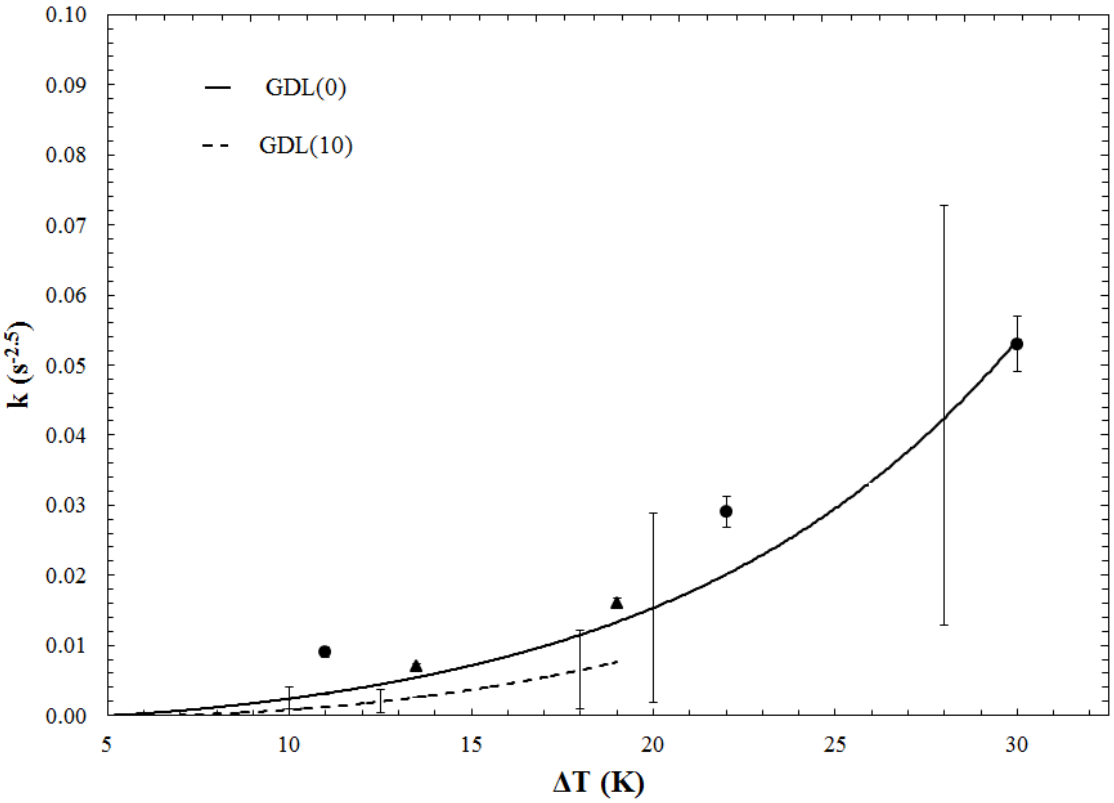

Figure 11. Overall rate constant, *k*, for GDL (0) (filled circles) and GDL(10) (filled triangles) as a function of subcooling. Filled symbols correspond to fitted values from eq 3. Solid and dashed lines are theoretical predictions of $k = (1 - f)k_O$ with $\alpha_l = 1.4 \times 10^{-7}$ m^2/s, $\theta_O = 60°$, an average value for J_O, and $f = 0$ and $f = 0.5$ for GDL(0) and GDL(10), respectively. Error bars on lines indicate the range of calculated *k* using the minimum and maximum J_O obtained from Figure 6.

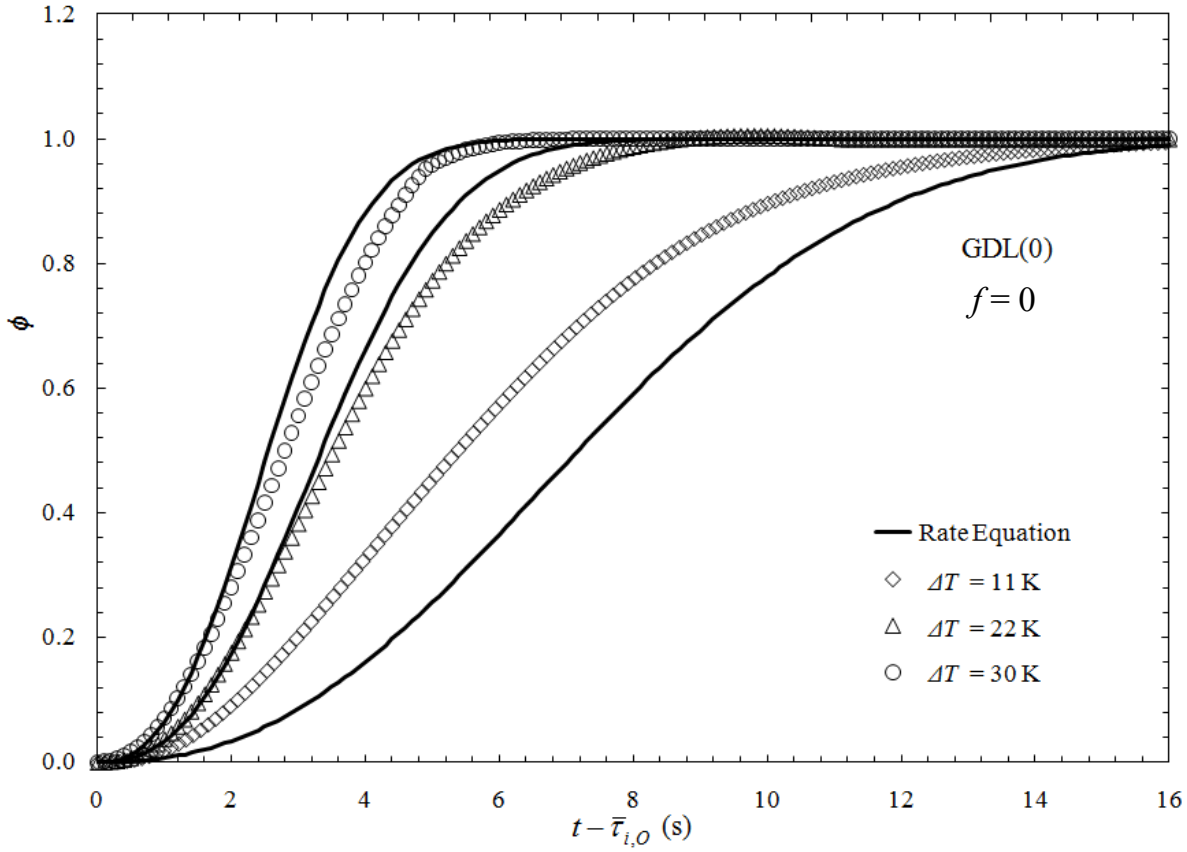

Figure 12. Isothermal freezing kinetics for the GDL(0) at three subcoolings. Solid lines represent theoretical predictions of ϕ using eq 10 and eq 12 for $k_O(T)$ with $\alpha_l = 1.4\times10^{-7}\,\mathrm{m^2/s}$, $\theta_o = 60°$, J_O from eq 17, η_o from eq 9, and $f = 0$.

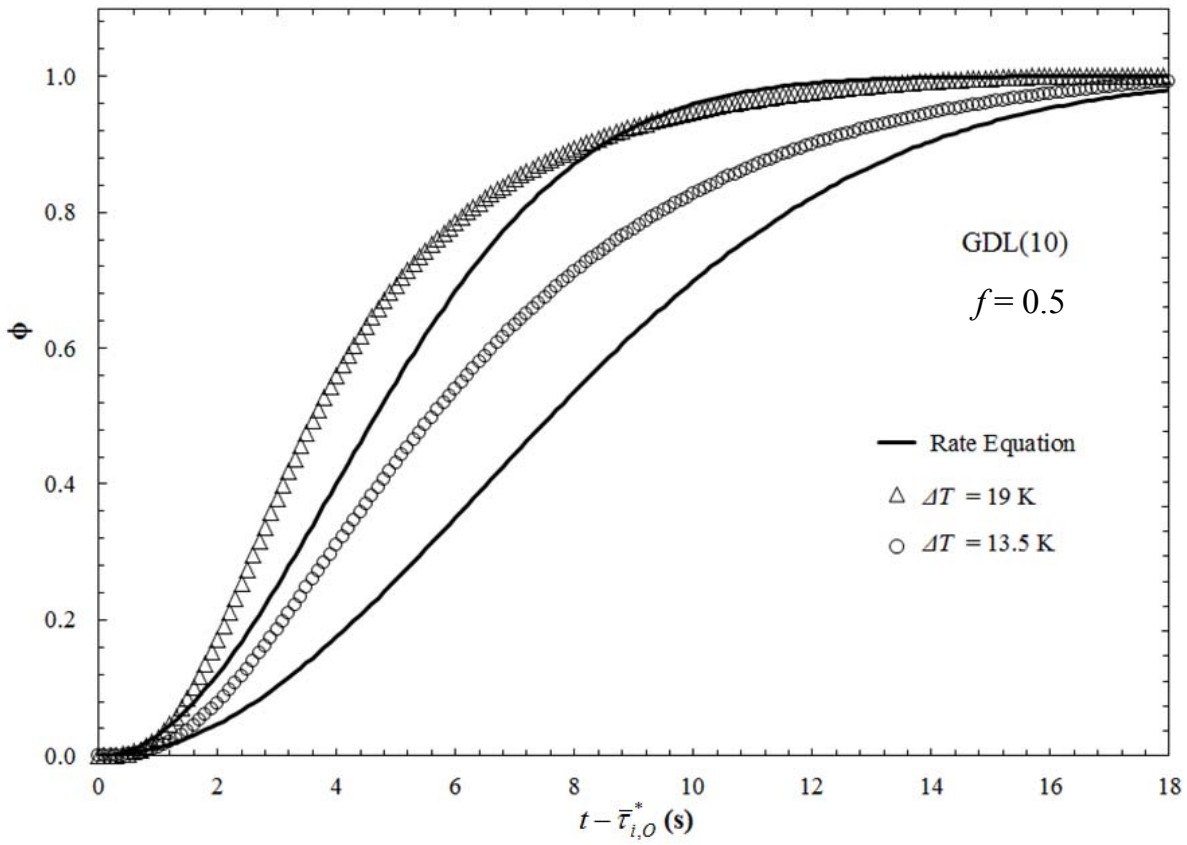

Figure 13. Isothermal freezing kinetics for the GDL(10) at two subcoolings. Solid lines represent theoretical predictions of ϕ using eq 10 and eq 12 for $k_O(T)$ with $\alpha_l = 1.4 \times 10^{-7}\,\mathrm{m^2/s}$, $\theta_o = 60°$, J_O from eq 17, and η_o from eq 9, and $f = 0.5$.

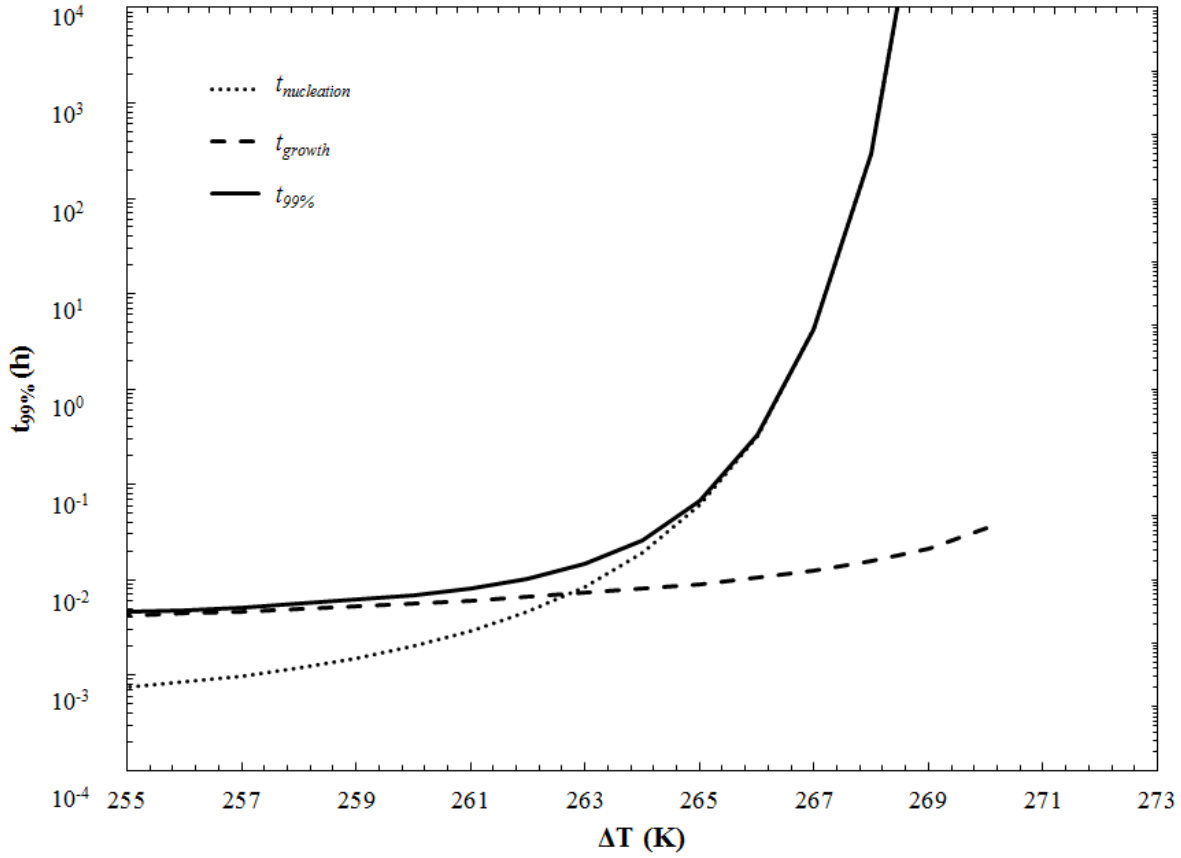

Figure 14. Time required for 99% crystallization as a function of temperature for the GDL(0). The dotted line estimates time required for the onset of crystallization, given by eq 20 with $f = 0$. The dashed line represents the time required (from the onset of crystallization) to form 99% of ice using eq 10 with $k_T(T) = 0$ and $k_o(T)$ given by eq 12. The solid line is the sum of the two dotted lines.